Monthly Notices of the ROYAL ASTRONOMICAL SOCIETY

MNRAS **507,** 1528–1545 (2021) https://doi.org/10.1093/mnras/stab1994
Advance Access publication 2021 July 21

First detection of VHE gamma-ray emission from TXS 1515–273, study of its X-ray variability and spectral energy distribution

MAGIC Collaboration,★ V. A. Acciari,[1] S. Ansoldi,[2] L. A. Antonelli,[3] A. Arbet Engels,[4] M. Artero,[5] K. Asano,[6] D. Baack,[7] A. Babić,[8] A. Baquero,[9] U. Barres de Almeida,[10] J. A. Barrio,[9] I. Batković,[11] J. Becerra González,[1] W. Bednarek,[12] L. Bellizzi,[13] E. Bernardini,[14] M. Bernardos,[11] A. Berti,[15] J. Besenrieder,[16] W. Bhattacharyya,[14] C. Bigongiari,[3] A. Biland,[4] O. Blanch,[5] Ž. Bošnjak,[8] G. Busetto,[11] R. Carosi,[17] G. Ceribella,[16] M. Cerruti,[18] Y. Chai,[16] A. Chilingarian,[19] S. Cikota,[8] S. M. Colak,[5] E. Colombo,[1] J. L. Contreras,[9] J. Cortina,[20] S. Covino,[3] G. D'Amico,[16] V. D'Elia,[3] P. Da Vela,[17]† F. Dazzi,[3] A. De Angelis,[11] B. De Lotto,[2] M. Delfino,[5,21] J. Delgado,[5,21] C. Delgado Mendez,[20] D. Depaoli,[15] F. Di Pierro,[15] L. Di Venere,[22] E. Do Souto Espiñeira,[5] D. Dominis Prester,[23] A. Donini,[2] D. Dorner,[24] M. Doro,[11] D. Elsaesser,[7] V. Fallah Ramazani,[25,26]★ A. Fattorini,[7] G. Ferrara,[3] M. V. Fonseca,[9] L. Font,[27] C. Fruck,[16] S. Fukami,[6] R. J. García López,[1] M. Garczarczyk,[14] S. Gasparyan,[28] M. Gaug,[27] N. Giglietto,[22] F. Giordano,[22] P. Gliwny,[12] N. Godinović,[29] J. G. Green,[3] D. Green,[16] D. Hadasch,[6] A. Hahn,[16] L. Heckmann,[16] J. Herrera,[1] J. Hoang,[9] D. Hrupec,[30] M. Hütten,[16] T. Inada,[6] S. Inoue,[31] K. Ishio,[16] Y. Iwamura,[6] I. Jiménez,[20] J. Jormanainen,[25] L. Jouvin,[5] Y. Kajiwara,[32] M. Karjalainen,[1] D. Kerszberg,[5] Y. Kobayashi,[6] H. Kubo,[32] J. Kushida,[33] A. Lamastra,[3] D. Lelas,[29] F. Leone,[3] E. Lindfors,[25]★ S. Lombardi,[3] F. Longo,[2,34] R. López-Coto,[11] M. López-Moya,[9] A. López-Oramas,[1] S. Loporchio,[22]★ B. Machado de Oliveira Fraga,[10] C. Maggio,[27] P. Majumdar,[35] M. Makariev,[36] M. Mallamaci,[11] G. Maneva,[36] M. Manganaro,[23] K. Mannheim,[24] L. Maraschi,[3] M. Mariotti,[11] M. Martínez,[5] D. Mazin,[6,16] S. Menchiari,[13] S. Mender,[7] S. Mićanović,[23] D. Miceli,[2] T. Miener,[9] M. Minev,[36] J. M. Miranda,[13] R. Mirzoyan,[16] E. Molina,[18] A. Moralejo,[5] D. Morcuende,[9] V. Moreno,[27] E. Moretti,[5] V. Neustroev,[37] C. Nigro,[5] K. Nilsson,[25] K. Nishijima,[33] K. Noda,[6] S. Nozaki,[32] Y. Ohtani,[6] T. Oka,[32] J. Otero-Santos,[1] S. Paiano,[3] M. Palatiello,[2] D. Paneque,[16] R. Paoletti,[13] J. M. Paredes,[18] L. Pavletić,[23] P. Peñil,[9] C. Perennes,[11] M. Persic,[2,38] P. G. Prada Moroni,[17] E. Prandini,[11] C. Priyadarshi,[5] I. Puljak,[29] W. Rhode,[7] M. Ribó,[18] J. Rico,[5] C. Righi,[3] A. Rugliancich,[17] L. Saha,[9] N. Sahakyan,[28] T. Saito,[6] S. Sakurai,[6] K. Satalecka,[14] F. G. Saturni,[3] B. Schleicher,[24] K. Schmidt,[7] T. Schweizer,[16] J. Sitarek,[12] I. Šnidarić,[39] D. Sobczynska,[12] A. Spolon,[11] A. Stamerra,[3] D. Strom,[16] M. Strzys,[6] Y. Suda,[16] T. Surić,[39] M. Takahashi,[6] F. Tavecchio,[3] P. Temnikov,[36] T. Terzić,[23] M. Teshima,[6,16] L. Tosti,[40] S. Truzzi,[13] A. Tutone,[3] S. Ubach,[27] J. van Scherpenberg,[16] G. Vanzo,[1] M. Vazquez Acosta,[1] S. Ventura,[13] V. Verguilov,[36] C. F. Vigorito,[15] V. Vitale,[41] I. Vovk,[6] M. Will,[16] C. Wunderlich,[13] D. Zarić,[29] E. Bissaldi,[42] G. Bonnoli,[13,43] S. Cutini,[44] F. D'Ammando,[45] A. Nabizadeh,[46] A. Marchini[47] and M. Orienti[45]

Affiliations are listed at the end of the paper

Accepted 2021 July 5. Received 2021 June 11; in original form 2021 March 19

ABSTRACT

We report here on the first multiwavelength (MWL) campaign on the blazar TXS 1515–273, undertaken in 2019 and extending from radio to very-high-energy gamma-rays (VHE). Up until now, this blazar had not been the subject of any detailed MWL

* Send offprint requests to MAGIC Collaboration (e-mail: contact.magic@mpp.mpg.de). Corresponding authors are S. Loporchio, E.Lindfors, and V. Fallah Ramazani.
† Present address: University of Innsbruck.

observations. It has a rather hard photon index at GeV energies and was considered a candidate extreme high-synchrotron-peaked source. MAGIC observations resulted in the first-time detection of the source in VHE with a statistical significance of 7.6σ. The average integral VHE flux of the source is 6 ± 1 per cent of the Crab nebula flux above 400 GeV. X-ray coverage was provided by *Swift*-XRT, *XMM–Newton*, and *NuSTAR*. The long continuous X-ray observations were separated by ∼9 h, both showing clear hour scale flares. In the *XMM–Newton* data, both the rise and decay time-scales are longer in the soft X-ray than in the hard X-ray band, indicating the presence of a particle cooling regime. The X-ray variability time-scales were used to constrain the size of the emission region and the strength of the magnetic field. The data allowed us to determine the synchrotron peak frequency and classify the source as a flaring high, but not extreme synchrotron-peaked object. Considering the constraints and variability patterns from the X-ray data, we model the broad-band spectral energy distribution. We applied a simple one-zone model, which could not reproduce the radio emission and the shape of the optical emission, and a two-component leptonic model with two interacting components, enabling us to reproduce the emission from radio to VHE band.

Key words: Radiation mechanisms: non-thermal – galaxies: active – objects: individual: TXS 1515–273.

1 INTRODUCTION

Almost all of the extragalactic sources detected above 100 GeV are classified as active galactic nuclei (AGNs): galaxies hosting a supermassive black hole in their centre whose gravitational potential energy is the ultimate source of the AGN luminosity. Up to ∼10 per cent of AGNs develop two narrow jets of relativistic particles extending well outside the galaxy and emitting non-thermal radiation over the whole electromagnetic spectrum (Padovani et al. 2017). The spectra observed from jetted-AGNs depend strongly on the viewing angle of the jet with respect to the Earth, leading to their empirical classification. Jetted-AGNs with jets seen from large angles are classified as radio galaxies, while those seen at small viewing angles ($\theta < 10^{\circ}$–15°) are known as blazars. Blazars' spectra are fully dominated by the jet emission, which can completely outshine the rest of the galaxy. They can be divided into flat spectrum radio quasars (FSRQs) and BL Lac objects (BL Lacs), depending on their optical spectra: FSRQs show strong, broad emission lines while BL Lacs display at most weak emission lines (Stickel et al. 1991; Stocke et al. 1991).

The broad-band spectral energy distribution (SED) of blazar emission is characterized by two distinct humps (Ghisellini et al. 2017). The first one peaks at infrared to X-ray frequencies and is commonly explained as due to synchrotron emission from ultra-relativistic electrons accelerated in the jet. The second hump, peaking above MeV energies, is most likely due to inverse Compton (IC) scattering, possibly of the same electrons on their own synchrotron emission (synchrotron self-Compton, SSC). The presence of a sub-dominant hadronic component is also possible, as discussed in Aharonian (2000) and Murase et al. (2012).

The energy of the synchrotron peak leads to a further sub-classification of blazars. The peak frequency ranges from IR–optical to UV–soft-X bands in low, intermediate, or high synchrotron-peaked sources (LSP, ISP, HSP, respectively, see Abdo et al. 2010). In particular, HSPs display a synchrotron emission peaking at frequencies $\nu_X \gtrsim 10^{15}$ Hz. Furthermore, evidence for objects with synchrotron peak frequency exceeding the HSP soft-X-ray band was found in Ghisellini (1999) and Costamante et al. (2001), with the most extreme high frequency-peaked blazars (EHBL) showing peaks above 10^{17} Hz (Costamante & Ghisellini 2002; Bonnoli et al. 2015) and a hard spectrum (photon index $\leq$2) at the *Fermi* Large Area Telescope (LAT) energies, with the IC peak generally in the energy range above 100 GeV. The origin of such an extreme peak exceeding TeV energies and an explanation for the hard intrinsic spectrum at sub-TeV energies are still widely debated. This feature indicates the presence of a hard accelerated particle spectrum with most of the energy carried by the highest energy particles.

As reported in Fossati et al. (1998), evidence of an empirical sequence connecting blazar classes with their bolometric luminosity was found, with LSP showing higher luminosity with respect to HSP blazars. The sequence was later revised by Ghisellini et al. (2017), finding good agreement with the original one. It is worth mentioning that the existence of the blazar sequence has been disputed ever since it was proposed, and it is still under debate (e.g. Keenan et al. 2020).

For any given blazar, only complete energy coverage, ranging from radio to TeV energies will allow for a robust study of the emission mechanisms. However, due to the variability of these objects, it is of crucial importance that these multiwavelength (MWL) observations are performed simultaneously.

Although reported in the Second and the Third Catalogue of AGNs detected by the *Fermi*-LAT (Ackermann et al. 2011, 2015), in the general *Fermi*-LAT catalogues (Nolan et al. 2012; Acero et al. 2015; Abdollahi et al. 2020) and in the high-energy catalogues (Ackermann et al. 2013, 2016; Ajello et al. 2017), the source TXS 1515–273 has been very little studied, and it has never been investigated intensively in the X-rays before the observations reported in this work. An upper limit on its redshift $z < 1.1$ was established in Kaur et al. (2018) with photometric methods. Recently, firm detection of spectral lines settled the redshift to $z = 0.1285$ (Becerra González et al. 2020; Goldoni et al. 2021).

In 3FGL and all prior *Fermi*-LAT catalogues the source had been indeed classified as a blazar candidate of uncertain type (Lefaucheur & Pita 2017) and only in 4FGL was it classified as a BL Lac object, with a photon index ≃2, which makes it an EHBL candidate (Abdollahi et al. 2020). EHBLs are of special interest in searching for new very-high-energy (VHE) gamma-ray blazars today as they are still rare and little studied (see e.g. Biteau et al. 2020). Some of them have shown a hard-TeV behaviour, with IC emission peaking above ∼ 10 TeV, while others were classified as EHBL showing extreme behaviour only during flares. According to Foffano et al. (2019) and Biteau et al. (2020), this may suggest the necessity for a classification of the EHBL class into different sub-classes.

Triggered by flaring activity in the high-energy gamma-ray band (HE, 0.5 MeV $\leq E \leq$ 100 GeV) reported by the *Fermi*-LAT (Cutini 2019), an MWL campaign on TXS 1515–273 was organized at the end of 2019 February. During the flaring activity, the source was observed in different energy bands, ranging from radio to VHE gamma-rays. Simultaneous or quasi-simultaneous observations were carried out by KVA, *Swift*, *XMM*, *Nuclear Spectroscopic Telescope Array* (*NuSTAR*), and Major Atmospheric Gamma-ray Imaging Cherenkov (MAGIC) in order to investigate the location of the

Table 1. Summary of the different observations performed.

Instrument	MJD start	MJD stop
MAGIC	58541.18	58547.21
Fermi-LAT	58540.72	58547.71
NuSTAR	58544.59	58545.31
XMM	58543.95	58544.21
Swift-XRT	58541.65	58560.71
Swift-UVOT	58541.65	58560.93
KVA	58541.22	58718.86
Siena	58542.17	58564.10

SED peaks and look for evidence of extreme behaviour during the flare. Following the observations, MAGIC announced the first-time detection of the source in the VHE band (Mirzoyan 2019). In this paper, we report the results of this observing campaign.

The paper is organized as follows. In Section 2, we describe the analysis in the different energy ranges and provide the results obtained. In Section 3, we present the studies of the MWL variability. In Section 4, we report on the detailed analysis of the available X-ray data sets, focusing on the short-time-scale variability and the spectral evolution. In Section 5, we describe the studies of the SED of TXS 1515–273, in particular its modelling and classification. Finally, in Section 6 we present our conclusions.

2 ANALYSIS RESULTS

Here, we present a summary of the MWL analysis performed on the acquired data. The list of the instruments and the relative time-range of observations are provided in Table 1. Further details on each data set are given in the following sections.

2.1 Very-high-energy gamma-rays

The MAGIC telescope (Aleksić et al. 2016) is a stereoscopic system of two 17-m diameter imaging atmospheric Cherenkov telescopes. MAGIC telescopes performed observations of TXS 1515–273 starting on 2019 February 27 (MJD 58541) up to 2019 March 5 (MJD 58547). The observations were performed at a high zenith angle, ranging from 55° to 62°, under both dark time (4.8 h) and moonlight conditions (3.3 h), implying a high night sky background level. For this reason, we optimized the analysis chain for data taken under moonlight conditions. For further details on the MAGIC performance under moonlight, refer to Ahnen et al. (2017). Data were analysed using the MAGIC analysis and reconstruction software MARS (Zanin et al. 2013). The observations led to a significant detection in the VHE range with a significance of 7.6σ. We derived the night-wise gamma-ray flux integrated above 400 GeV. The MAGIC observed flux is reported in Table A1.

Since the acquired signal was not strong enough to evaluate the spectrum for each night, we combined all the data to obtain the overall spectrum. We fitted it with a power-law function, folded with the energy dispersion using the Bertero unfolding method (Bertero 1989) and corrected for gamma-ray absorption by the interaction with the extra-galactic background light (EBL) using the Domínguez et al. (2011) model. After the unfolding and the EBL correction, the MAGIC soft spectrum between 200 and 900 GeV is well described by a power-law model:

$$\frac{\mathrm{d}N}{\mathrm{d}E} = N_0 \left(\frac{E}{E_0}\right)^{-\Gamma}, \quad (1)$$

where $\Gamma = 3.11 \pm 0.32_{\mathrm{stat}}$ is the photon index, $E_0 = 546\,\mathrm{GeV}$ is the normalization energy, selected as the decorrelation energy and $N_0 = (1.76 \pm 0.28_{\mathrm{stat}}) \times 10^{-11}\,\mathrm{TeV}^{-1} \cdot \mathrm{cm}^{-2} \cdot \mathrm{s}^{-1}$ is the corresponding normalization constant. The systematic uncertainties of the MAGIC telescopes are below 15 per cent on the absolute energy scale, 11–18 per cent on flux normalization, and ±0.15 on the spectral slope (Aleksić et al. 2016). The soft spectrum in the VHE range suggests that the IC bump is likely peaking at GeV energies, as discussed in Section 5.3.

2.2 High-energy gamma-rays

The Large Area Telescope (LAT) instrument onboard the *Fermi Gamma-Ray Space Telescope* satellite is a pair-conversion telescope with a precision converter-tracker and calorimeter that detects gamma-rays (Atwood et al. 2009).

Data from the `Source` event class were analysed using the Fermitools v1.2.1 and the `fermipy`[1] v0.18 python package, applying standard quality cuts (`'DATA_QUAL>0 && LAT_CONFIG==1'`) and the zenith distance cut (<90°) to reduce the Earth limb contamination. Only events with reconstructed energy in the 300 MeV–500 GeV range within 12° of the nominal position of the studied source were selected. A time window of 7 d between 2019 February 27 (MJD 58541) and 2019 March 5 (MJD 58547) was selected in temporal coincidence with MAGIC observations to evaluate the measured flux as a function of the time. A different time selection, from 2019 February 27 up to and including 2019 March 3 (MJD 58545) was selected for the spectral analysis, for reason that will be explained in detail in Section 5.3. A binned likelihood analysis was performed with 8 bins per energy decade for the selected region of interest. The instrument response function used was P8R3_SOURCE_V2. All of the sources in the 4FGL catalogue (Abdollahi et al. 2020) were included in the model, along with the isotropic (`iso_P8R3_SOURCE_V2_v1`) and the Galactic (`gll_iem_v07`) models (Acero et al. 2016).[2]

In the fitting procedure, the spectral parameters of sources that are significantly detected within a radius of 5° around the source of interest were left free together with the normalization of the diffuse components. All of the other catalogue sources' parameters were fixed to the published 4FGL values. A dedicated likelihood analysis was performed for each time bin. The resulting light curve in daily bins is shown in Fig. 1, while the observed flux and the test statistic (TS) in each time bin are reported in Table A2.

The average spectrum obtained from *Fermi*-LAT data is described by a power-law model, with the following spectral parameters: $N_0 = (20.5 \pm 7.2) \times 10^{-13}\,\mathrm{MeV}^{-1} \cdot \mathrm{cm}^{-2} \cdot \mathrm{s}^{-1}$, $\Gamma = 2.2 \pm 0.3$ and $f_{\mathrm{E>300\,MeV}} = (4.5 \pm 1.3) \cdot 10^{-8}\,\mathrm{cm}^{-2}\,\mathrm{s}^{-1}$ GeV, with $E_0 = 2.3$ GeV.

2.3 X-rays

Following the detection of the source at VHE gamma-rays, TXS 1515–273 was observed at X-ray energies with the *NuSTAR* telescope, the *XMM–Newton* observatory, and the *Neil Gehrels Swift observatory*. In this section, we will present these observations and their outcomes.

[1] https://fermipy.readthedocs.io/en/latest/

[2] https://fermi.gsfc.nasa.gov/ssc/data/analysis/software/aux/4fgl/Galactic_Diffuse_Emission_Model_for_the_4FGL_Catalog_Analysis.pdf

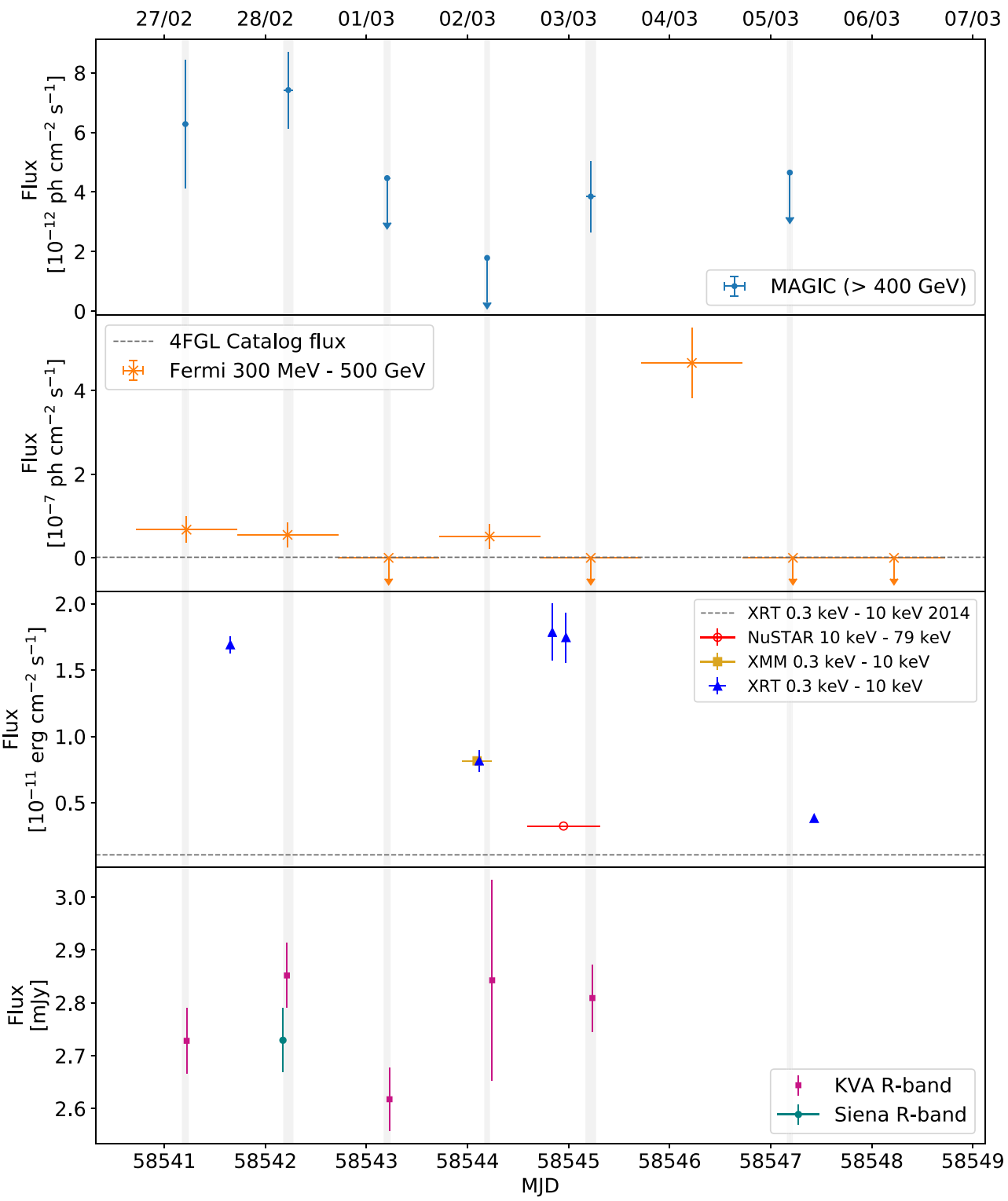

Figure 1. MWL light curve of TXS 1515–273 from 2019 February 27 to 2019 March 6. From top to bottom: VHE gamma-rays by MAGIC, HE gamma-rays by *Fermi*-LAT, X-rays by *Swift*-XRT (blue triangles), *NuSTAR* (red open circles), and *XMM–Newton* (yellow squares) in different energy bands and R-band by KVA and Siena observatory. 95 per cent confidence upper limits are indicated as downward arrows in VHE gamma-rays where the flux is compatible with zero as well as in the HE band for each time bin where the TS value for the source was found to be smaller than 9. The individual light curves are daily binned. Dashed horizontal grey lines indicate the level of detected flux during 2014 *Swift*-XRT observations and the reference flux level in the 4FGL catalogue. The grey vertical bands are drawn to highlight the MAGIC observation time slots. Magnitudes for optical data were corrected for Galactic extinction, and the host galaxy contribution was subtracted (details in the text).

2.3.1 XMM–Newton *observation*

The *XMM–Newton* observatory (Jansen et al. 2001) is a space-based X-ray observatory that carries three medium spectral resolution X-ray telescopes, two Reflection Grating Spectrometers for high resolution spectroscopy (Den Herder et al. 2001), and a 0.3-m optical/UV imaging telescope onboard (see Section 2.4.2). The three X-ray telescopes at the focus of the European Photon Imaging Camera (EPIC; 0.2–10 keV) are a pn-CCD operating in full frame mode (Strüder et al. 2001) and two multi-object spectrometer CCDs (MOS1 and MOS2) operating in small-window mode (Turner et al. 2001).

The ToO *XMM–Newton* observation of TXS 1515–273 closest to our campaign was performed at the beginning of 2019 March 2 for ∼25 ks of exposure time with the three X-ray telescopes. Using the *XMM–Newton* Science Analysis System SAS version 17.0.0 and the latest available calibration files, we reduced and analysed the data by following the standard procedure explained in the SAS user guide.[3] The source spectra were extracted from a source-centred circular region with a radius of 35 arcsec for all three instruments to have the best signal-to-noise ratio. The background spectra likewise were extracted from source-free regions on the same chips. We also used a time filter expression to divide the whole observation into short segments with durations of 300 s. Then we extracted the final corresponding spectra from these segments to study the source variation over shorter time-scales.

In order to estimate the Galactic column density of Hydrogen ($N_{\rm H}$) in the direction of the source, we used the full data set obtained by all three X-ray instruments onboard of *XMM–Newton*. The spectra are binned in a way that each spectral bin contains 20 counts. The joint fit of the spectra is done using XSPEC V12.10.1S, using photon absorption model folded with a power-law and log-parabola model, while the $N_{\rm H}$ was set as a free parameter in our analysis. Moreover, the model was multiplied by a constant to account for the cross-calibration between the three instruments. The multiplicative factor was fixed to 1 for the EPIC-pn and left as free parameter in the models which are used for MOS1 and MOS2. The observed spectrum can be described well by a power-law model with photon index $\Gamma_{\rm XMM} = 2.53 \pm 0.01$ ($\chi^2/d.o.f. = 2019/1882$). We found that the log-parabola model cannot describe the observed spectrum better than the power-law model. The cross-calibration factor between the instruments was below 2 per cent. The value for the Galactic column density of Hydrogen from our spectral analysis is $N_{\rm H} = (1.68 \pm 0.03) \times 10^{21}$ cm^{-2}. The estimated value of $N_{\rm H}$ is in agreement with the results presented in Willingale et al. (2013). Therefore, the Galactic column density of Hydrogen is fixed to the estimated $N_{\rm H}$ value in the spectral analysis with shorter time bins and for the analysis of data from other X-ray instruments. The observed flux with *XMM–Newton* is reported in Table A3.

2.3.2 NuSTAR *observation*

The *NuSTAR* carries two co-aligned grazing incidence X-ray telescope systems, Focal Plane Module A and B (FPMA and FPMB), operating in a wide energy range of 3–79 keV (Harrison et al. 2013). These independent CdZnTe detector units provide X-ray imaging resolution of 18 arcsec (full width at half-maximum, FWHM) and spectral resolution of 400 eV (FWHM) at 10 keV. The *NuSTAR* ToO observation of TXS 1515–273 was performed at the end of 2019 March 2 (∼9 h after the end of *XMM–Newton* observation) for a 34 ks exposure time. The data reduction and product extraction were done using the *NuSTAR* Data Analysis Software NUSTARDAS V1.8.0 with a CALDB version 20180419. We performed the standard data reduction procedure explained in the *NuSTAR* user guide.[4] In order to extract the source spectrum, a source-centred circular region with a radius of 30 arcsec was used for both FPMA and FPMB. Likewise, the background was extracted from a source-free region with a larger radius of 60 arcsec. By creating user-selected good time intervals, we divided each exposure into six segments which enabled us to extract the spectra with durations of about 500–600 s each.

We fitted both spectra collected from FPMA and FPMB simultaneously in XSPEC V12.10.1S using a cross-calibration normalization for each segment of observations. Due to the low count rate, we grouped all of the X-ray spectra to have at least 1 count per each energy bin. We then took the W-statistics (Wachter, Leach & Kellogg 1979) into account to do the fitting procedure. The photon absorption model folded with a power law is used by assuming a fixed $N_{\rm H}$, which was estimated in Section 2.3.1. The cross-calibration factor was always below 3 per cent. The results of this analysis are presented in Section 4. The *NuSTAR* observed flux is reported in Table A4.

2.3.3 Swift-*XRT observations*

The *Neil Gehrels Swift (Swift)* satellite (Gehrels et al. 2004) carried out eight observations of TXS 1515–273 between 2014 September 30 and 2019 March 18. The observations were performed with all three instruments onboard: the X-ray Telescope (XRT; Burrows et al. 2005, 0.2–10.0 keV), the Ultraviolet/Optical Telescope (UVOT; Roming et al. 2005, 170–600 nm) (see Section 2.4.1), and the Burst Alert Telescope (BAT; Barthelmy et al. 2005, 15–150 keV). The hard X-ray flux of this source turned out to be below the sensitivity of the BAT instrument for such short exposures and therefore the data from this instrument will not be used. Moreover, the source was not included in the *Swift*-BAT 70-month hard X-ray catalogue (Oh et al. 2018).

The multi-epoch event lists of the *Swift*-XRT data were downloaded from the publicly available *Swift*-XRT Instrument Log.[5] These observations were carried out in photon-counting mode. Following the standard *Swift*-XRT analysis procedure described by Evans et al. (2009), the data were processed using the configuration described by Fallah Ramazani, Lindfors & Nilsson (2017) for blazars, assuming a photon absorption model folded with a power-law model and fixed $N_{\rm H}$ as estimated in Section 2.3.1. In Table A5, we provide the results obtained from fitting the *Swift*-XRT spectrum.

Two *Swift*-XRT snapshots (MJD 58544.84 and 58544.97), simultaneous with the *NuSTAR* data, are combined with each other. A joint fit was performed using these XRT data set and the full data obtained by *NuSTAR*. The observed spectra can be described by a photon absorption model (assuming fixed $N_{\rm H}$) folded with a broken power-law model ($\chi^2/d.o.f. = 405/378$). The spectrum shows a break at 3.34 ± 0.34 keV. The photon indexes before and after the break energy are $\Gamma_1 = 2.10 \pm 0.11$ and $\Gamma_2 = 2.72 \pm 0.03$, respectively. The cross-calibration factor between *Swift*-XRT and *NuSTAR* data was 15 per cent.

[3] https://xmm-tools.cosmos.esa.int/external/xmm_user_support/documentation/sas_usg/USG/

[4] https://nustar.ssdc.asi.it/news.php#

[5] https://heasarc.gsfc.nasa.gov/W3Browse/swift/swiftxrlog.html

2.4 Optical and UV

2.4.1 Swift-*UVOT observations*

During the *Swift* pointings, the UVOT instrument observed TXS 1515–273 in all of its optical (v, b and u) and UV ($w1$, $m2$, and $w2$) photometric bands (Poole et al. 2008; Breeveld et al. 2010). We analysed the data using the `uvotsource` task included in the`HEASOFT` package (v6.28) with the 20201026 release of the Swift/UVOTA CALDB. Source counts were extracted from a circular region of 5 arcsec radius centred on the source, while background counts were derived from a circular region of 20 arcsec radius in a nearby source-free region. The observed magnitudes are reported in Table A9.

The UVOT flux densities were corrected for Galactic extinction using the E(B–V) value of 0.209 from Schlafly & Finkbeiner (2011) and the extinction laws from Cardelli, Clayton & Mathis (1989). From the V-band fluxes, we subtracted the host galaxy contribution, which was estimated assuming a host galaxy absolute magnitude $M_R = -22.8$, galaxy colour V–R = 0.8 (Fukugita, Shimasaku & Ichikawa 1995), and $z = 0.1285$. Within the aperture of 5 arcsec, its contribution is 0.13 mJy. We corrected only the V-band because the host galaxy contribution to other UVOT bands is negligible. We note that the magnitudes in Table A9 are the observed ones, i.e. corrections for neither the host galaxy contribution nor the Galactic extinction have been performed.

2.4.2 XMM-OM *observations*

The Optical Monitor (OM) observed the source in the b, u, and $w1$ filters in imaging mode. The total exposure times of the imaging observations are approximately: 9400, 4700, and 9400 s. The data were processed using the SAS task `omichain`. The count rate is converted to flux using the conversion factors given in the SAS watchout dedicated page.[6] The observed magnitudes with *XMM-OM* are reported in Table A6. These magnitudes were then corrected for extinction using the same E(B–V) value and extinction laws as for the UVOT data.

2.4.3 KVA

The optical R-band observations were performed using the 35-cm telescope attached to the 60-cm KVA telescope located at La Palma. The data analysis was performed using the standard procedures with the semi-automatic pipeline developed in Tuorla (Nilsson et al. 2018). As the source is not part of the Tuorla Blazar monitoring program,[7] a proper calibration was required in order to perform differential photometry. A comparison star and a control star were selected among known stars in the same field of view and were calibrated with respect to stars in the field of other targets observed on the same night under photometric conditions.

The magnitudes were corrected for Galactic extinction using the same E(B–V) value as for correcting the UVOT data. The host galaxy flux was estimated in the same way as for the UVOT, resulting in a contribution of 0.303 mJy within the used aperture of 5 arcsec.

Observations of the source were performed for several months after the flaring state to estimate the flux during quiescent periods. The overall light curve is reported in Fig. 2, while the observed magnitudes (without host galaxy subtraction or Galactic extinction corrections) are reported in Table A8.

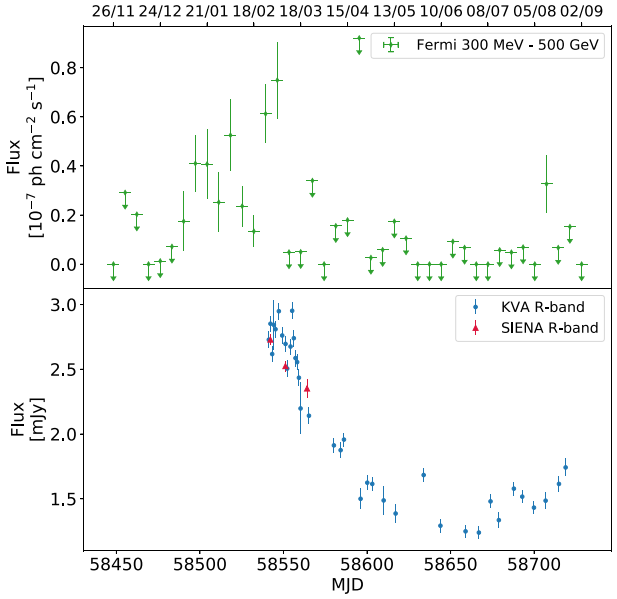

Figure 2. HE gamma-ray (top, green diamonds) and R-band (bottom, KVA in blue circles and Siena observatory in red triangles) light curves of TXS 1515–273. *Fermi*-LAT light curve is shown in weekly bins, with 95 per cent confidence UL indicated. The light curve starts from a few months before the flare period up to 2019 August. The large flare can be seen during our observations. The optical light curve has daily bins, starting from the observations carried out during the flare.

2.4.4 Siena

The Astronomical Observatory of the University of Siena observed TXS 1515–273 in the context of a program focused on optical photometry of blazars in support of MAGIC. The instrumentation consists of a remotely operated 30-cm Maksutov-Cassegrain telescope installed on a Comec 10 micron GM2000-QCI equatorial mount. The detector is a Sbig STL-6303 camera equipped with a 3072 × 2048 pixels KAF-6303E sensor; the filter wheel hosts a set of Johnson–Cousins BVRI filters. Multiple 300 s images of TXS 1515–273 were acquired in the R band at each visit. Observations were always performed closely around culmination given the southern declination of the source. After standard dark current subtraction and flat-fielding, images for each visit were averaged and aperture photometry was performed on the average frame by means of the MaximDL software package. The choice of reference and control stars was consistent with the one for the KVA data. The obtained magnitudes reported in Table A7 were corrected for Galactic extinction and the host galaxy magnitude, which results in a contribution of 0.37 mJy within the used aperture of 7 arcsec, was subtracted as was done for the KVA data. Table A7 reports the magnitudes without these corrections.

2.5 Very Long Baseline Array

TXS 1515–273 has been observed six times with the Very Long Baseline Array (VLBA) Experiment (Lister et al. 2019) at 15 GHz as part of the Monitoring Of Jets in Active galactic nuclei with VLBA

[6] https://www.cosmos.esa.int/web/xmm-newton/sas-watchout-uvflux
[7] http://users.utu.fi/kani/1m/index.html

Experiments (MOJAVE) program[8]. It was observed three times in 2017 (January 28, May 25, and June 17), once in 2018 (May 31) and twice in 2019 (June 13 and July 19). We retrieve the fully calibrated MOJAVE data sets and we produced images in Stokes' I, Q, and U using the task IMAGR in AIPS. We then combined images in Stokes Q and U and produced polarization intensity images and the associated error maps. We fitted the visibility data with circular Gaussian components at each epoch using the model-fit option in DIFMAP. Model-fitting the visibility reveals the core and two quasi-stationary components: the first one at 0.15–0.2 milliarcsec from the core and the second one at 1.5 milliarcsec (both with a nearly constant flux). From the data, there is no evidence for a new jet component emerging from the core, but the cadence of the observations is not optimal for detecting new components. The core flux was almost constant within the error bars, varying between 81 ± 6 (2019 June) and 99 ± 7 mJy (2017 May), in the first five epochs, while in the last epoch (2019 July) there is marginal hint of increased flux (109 ± 8 mJy).

The source was not polarized in 2017 with an upper limit to the polarized flux density ≤0.2 mJy and to the fractional polarization ≤0.15 per cent. In 2018 May, the polarized flux increased to 0.8 ± 0.1 mJy, corresponding to a fractional polarization of 0.5 per cent. In 2019, the polarized flux increased again to 1.5 ± 0.2 mJy (about 1.5 per cent) and 1.0 ± 0.1 mJy (0.8 per cent) in June and July, respectively. However, the sparse time coverage does not allow us to set any robust connection between the polarized emission and the MWL activity.

3 MULTIWAVELENGTH VARIABILITY

The light curves of TXS 1515–273 in the different wavelengths from radio to VHE gamma-rays are reported in Fig. 1. The MWL light curves include all observations from MJD 58541 to MJD 58548. For comparison purposes, we show dashed grey lines in the *Fermi*-LAT and *Swift*-XRT light curves representing the reference value flux from the 4FGL catalogue (Abdollahi et al. 2020) and a previous detection from *Swift*-XRT. From the reference level of the 4FGL catalogue and a previous observation in the X-rays, it is evident that the source was in a high state in the X-ray and the HE band. The long term optical and HE gamma-ray light curves shown in Fig. 2 also indicate clearly that the observed flux in those energy ranges was higher than usual. A significant increase of activity was also observed by *Swift*-UVOT between 2014 and 2019 with all optical and UV filters (see Table A9).

The *Fermi*-LAT light curve shows a significantly higher flux in HE during the night of 2019 March 4, when the MAGIC observations in VHE gamma-rays were prevented by bad weather. The *Fermi*-LAT SED was evaluated up to and including the night of 2019 March 3, to exclude this high state for which we did not have MAGIC data (see Fig. 1 and Section 5.3).

We also searched for intra-night variability in different bands. Intra-night variability was detected in X-ray observations on 2019 March 2 with both *XMM–Newton* and *NuSTAR*. The longest continuous MAGIC observations were ∼2 h, but due to lack of statistics we could not investigate further for intra-night variability. In the *Fermi*-LAT band, the source is too weak to detect hour-scale variability as found in X-ray band. In optical band, the variability in general has a rather small amplitude. We remark, however, that the *XMM–Newton* and *NuSTAR* observations, despite being very close in time, were not overlapping: as a result, different variability time-scales are not

[8]https://www.physics.purdue.edu/MOJAVE/

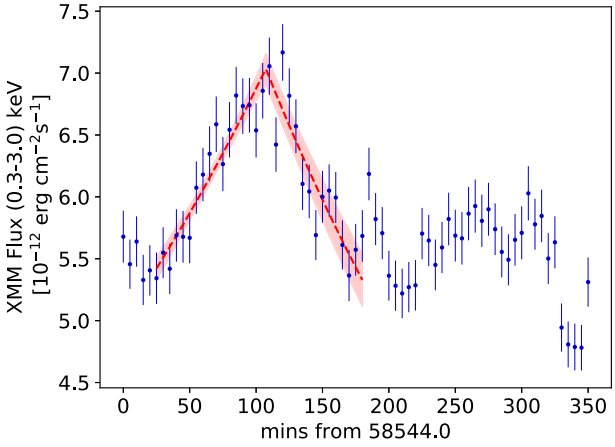

(a) *XMM-Newton* 0.3 – 3 keV 5-minute bins light curve for TXS 1515–273.

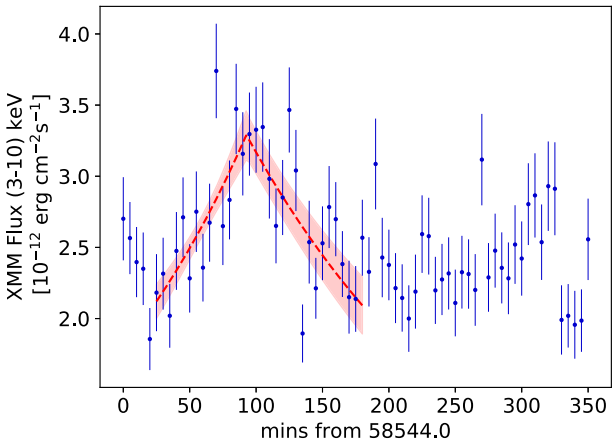

(b) *XMM-Newton* 3 – 10 keV 5-minute bins light curve for TXS 1515–273.

Figure 3. *XMM–Newton* light curves for TXS 1515–273 for soft (top) and hard (bottom) energy band. The dashed curves superimposed on the data represent the exponential function used to fit the peak, the rise and decay time of the bursts. The red shaded areas represent the uncertainties of the fit.

unexpected, as indeed was found (see Section 4). Consequently, we also decided to model the SED separately for the *XMM–Newton* and *NuSTAR* epochs, as we will discuss in detail in Section 5.3.

4 SHORT-TIME X-RAY VARIABILITY

Our observing campaign had particularly good coverage in X-rays, including *XMM–Newton*, *Swift*-XRT, and *NuSTAR*. The long exposures of *XMM–Newton* and *NuSTAR* observations allow us to investigate in detail the short-time-scale variability of the source in X-rays.

4.1 Flare time-scales

The light curves showed multiple flares (see Figs 3 and 4) and in the following we investigate the details of this variability and use it to constrain physical parameters of the emission region.

To constrain the variability time-scale, an exponential function in the form

$$F(t) = A \cdot \begin{cases} \exp[(t - t_{\rm peak})/t_{\rm rise}] & \text{if} \quad t < t_{\rm peak} \\ \exp[(t_{\rm peak} - t)/t_{\rm decay}] & \text{if} \quad t > t_{\rm peak} \end{cases} \tag{2}$$

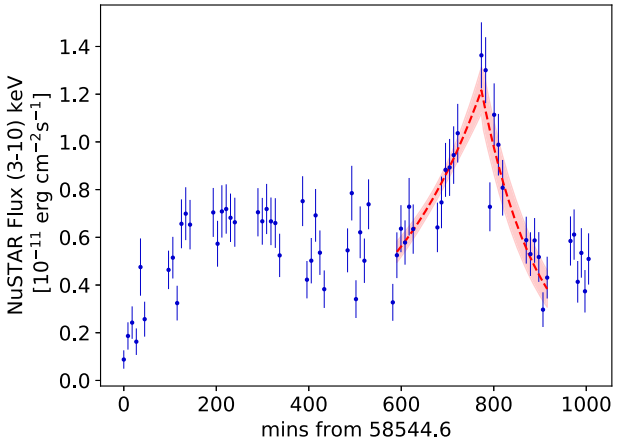

(a) *NuSTAR* 3 – 10 keV 10-minute bins light curve for TXS 1515–273.

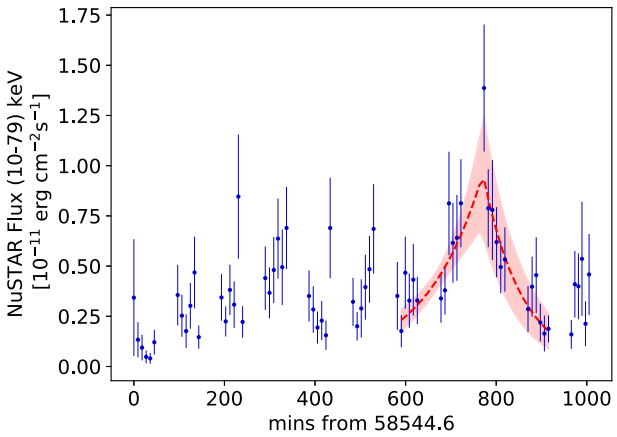

(b) *NuSTAR* 10 – 79 keV 10-minute bins light curve for TXS 1515–273.

Figure 4. *NuSTAR* light curves for TXS 1515–273 for soft (top) and hard (bottom) energy band. The dashed curves superimposed on the data represent the exponential function used to fit the peak, the rise and decay time of the bursts. The red shaded areas represent the uncertainties of the fit.

was used to fit the peak time, the rise and fall profiles of the bursts visible in the light curves. In both epochs, we fitted the soft and the hard energy band light curves independently, as shown in Figs 3 and 4.

The results of the fit are reported in Table 2. We cross-checked the results of our fit with different time binning of the light curves, i.e. 5, 10, and 15 min for *XMM–Newton* and ∼10 and ∼20 min for *NuSTAR*. As a confirmation of the consistency of the results, no significant difference was found for the different binning.

We also tried several combinations for start and stop bins. First, we selected a reasonable range for them to vary, performing the fit of the flare profile with different combinations of the range edges. We always kept the same fit range for soft and hard light curves. Finally, we picked the range that gave the best agreement with experimental data, i.e. with the minimum χ^2 value. The parameter $t_{\rm peak}$ was always set free to vary during the fitting procedure.

As shown in Figs 3 and 4, rapid variations on the time-scale of the order of hours were detected in the two epochs. The derived time-scales are not anomalous compared to X-ray flares seen in other blazars (MAGIC Collaboration 2020a, c).

The flare profiles in all bands are symmetric, i.e. within the derived error bars the rise and decay time-scales of the flares are not significantly different. The rise times of both the observed X-ray flares are longer in the low-energy band than in the high-energy band. The difference is significant both in the *XMM–Newton* and *NuSTAR* results, with a confidence level higher than 99 per cent and 90 per cent for the two data sets, respectively. In standard acceleration scenarios, low-energy electrons are supposed to be accelerated faster than high-energy ones. If the rise-time of the flare is dominated by the acceleration time-scale, then the rise-time in the lower energy band is expected to be shorter than the one in the high-energy band. However, higher energy electrons cool faster than lower energy electrons, and therefore in a cooling dominated regime one would indeed expect the higher energies to rise faster (e.g. Kirk, Rieger & Mastichiadis 1998) as seen in our data. This should also result in the high-energy flux peaking earlier than the lower energy flux, as seen in *XMM–Newton* data. In *NuSTAR* data, this is not evident, which is in line with lower statistical significance in difference of rise times between the two bands as well.

4.2 Spectral evolution

We investigated the dependence of the photon index on the flux in the full energy range (0.3–10 keV for *XMM–Newton*, 3–79 keV for *NuSTAR*). The *XMM–Newton* photon index showed little variations, ranging between 2.35 ± 0.05 and 2.76 ± 0.06 (using 5-min binning within the full time range of observation), while the *NuSTAR* photon index showed a wider dynamical range, varying between 2.01 ± 0.26 and 4.33 ± 0.71 (using 10-min binning within the full time range of observation). In both of the epochs studied, this dependence showed a more complicated behaviour than simple spectral hardening. We also examined the relation between the integral flux and the hardness ratio, but no clear correlation between these quantities was found in our data sample.

We then focused our search on the most prominent flares in the X-ray light curves (i.e. the one we also used to constrain the variability time-scale), see Fig. 5. We slightly narrowed the time window with respect to the time range shown in red in Figs 3 and 4 focusing on the most prominent flare time slots, MJD 58544.00–58544.08, (i.e. 25–125 min after the beginning of the observations) for *XMM–Newton* and MJD 58545.08–58545.17, (i.e. 670–810 min after the beginning of the observations) for *NuSTAR*. In this time epoch, the data are statistically consistent with a simple harder-when-brighter

Table 2. Results of the fit of the burst profile for the *XMM–Newton* and the *NuSTAR* epoch. The starting time corresponds to MJD 58543.0 for *XMM–Newton* and to MJD 58544.6 for *NuSTAR*.

Instrument and energy	$t_{\rm rise}$ (min)	$t_{\rm peak}$ (min)	$t_{\rm decay}$ (min)	$t_{\rm peak}$ (MJD)
XMM (0.3–3 keV)	316 ± 34	107 ± 3	262 ± 32	58544.06
XMM (3–10 keV)	159 ± 29	93 ± 6	193 ± 37	58544.06
NuSTAR (3–10 keV)	225 ± 42	773 ± 10	123 ± 17	58545.14
NuSTAR (10–79 keV)	127 ± 41	771 ± 16	86 ± 18	58545.14

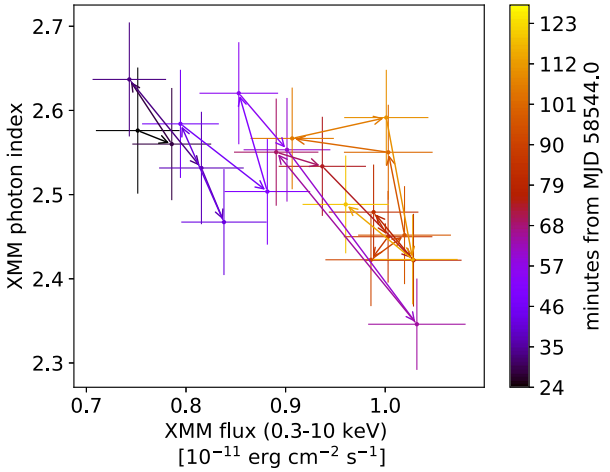

(a) *XMM-Newton* photon index versus integral (0.3 - 10 keV) flux for TXS 1515–273 during the short flare observed (MJD 58544.00 - 58544.08, i.e. 25 - 125 minutes after the beginning of the observations).

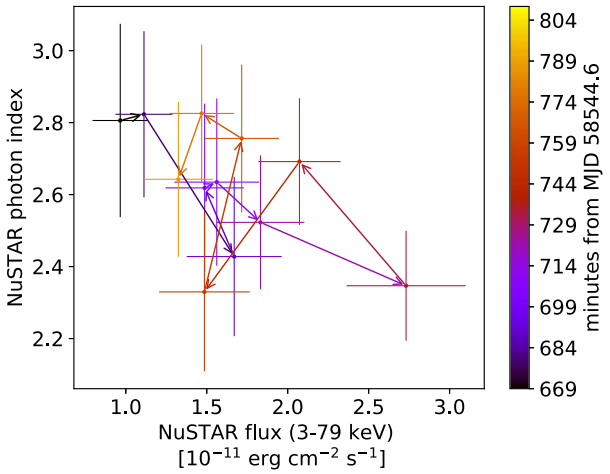

(b) *NuSTAR* photon index versus integral (3 - 79 keV) flux for TXS 1515–273 during the short flare observed (MJD 58545.08 - 58545.17, i.e. 670 - 810 minutes after the beginning of the observations).

Figure 5. *XMM–Newton* (top) and *NuSTAR* (bottom) photon index versus integral flux for TXS 1515–273 during short X-ray flares. The coloured arrows represent the time evolution.

trend. Indeed, we fitted the data in both epochs with a linear function and we found that the reduced χ^2 is 0.97 for the *XMM–Newton* flare and 0.55 for the *NuSTAR* flare.

4.3 Constraints on emitting region parameters from variability time-scales

Using the shortest time-scale from these variability studies for individual epochs, the size of the emission region can be constrained as a function of the Doppler factor δ:

$$R \leq \frac{c t_{\rm var} \delta}{(1+z)}, \tag{3}$$

where we used $t_{\rm var} = 159 \pm 29$ min for the *XMM–Newton* epoch and $t_{\rm var} = 86 \pm 18$ min for the *NuSTAR* epoch (see Table 2).

Since we have no strong constraints on the Doppler factor neither from our observing campaign nor from the previous observations of the source, we used $\delta \sim 20$ first, but then iterated the value during the SED modelling (see Section 5.3). The values close to 20 are rather typical for VHE gamma-ray emitting BL Lacs (Tavecchio et al. 2010).

Table 3. Results of the variability time-scale fit and estimation of R and B.

Epoch	δ	R ($\times 10^{15}$cm)	B (G)
XMM	20	5.07 ± 0.92	0.14 ± 0.02
NuSTAR	20	2.73 ± 0.58	

As we were able to constrain the variability time-scales in both epochs in the two different energy bands, we followed Zhang et al. (2002) to use these time-scales to constrain the magnetic field strength of the emission region. The synchrotron cooling time of electrons is inversely proportional to the square root of the energy of the photons. Indeed, the results of our fit are consistent with this scenario, as we find the *XMM–Newton* lower energy photons cooling time is longer than the one found for the *NuSTAR* higher energy ones.

The magnetic field strength is then calculated using the formula from Zhang et al. (2002):

$$B = 210 \left(\frac{1+z}{E_l \times \delta}\right)^{1/3} \left[\frac{1-(E_l/E_h)^{1/2}}{\tau_{\rm soft}}\right]^{2/3} \ {\rm G} \tag{4}$$

where E_l and E_h are taken as the logarithmic mean energies in the low and high-energy band in units of keV for the low-energy band and the high-energy band considered, and $\tau_{\rm soft}$ is the difference in the decay time values for the energy bands considered. We decided to combine the observations from the two epochs because the time lag in our observations is not statistically significant. By working under the assumption that the magnetic field does not vary between the two epochs, we used the low-energy band of *XMM–Newton* and the high-energy band of *NuSTAR*, and $\tau_{\rm soft} = t_{\rm decay,XMM} - t_{\rm decay,NuSTAR} = 10.56 \pm 2.20$ ks.

The upper limit value of R and the estimated value of B corresponding to $\delta = 20$ obtained with the variability time-scales estimated from the two epochs are reported in Table 3. These values were used to model the SED, as we will describe in Section 5.3.

5 SPECTRAL ENERGY DISTRIBUTION

In this campaign, we measured the SED of TXS 1515–273 for the first time from the optical to the VHE gamma-ray band. This allowed us to investigate the source classification and possible emission models during the flaring state.

5.1 Source classification

As reported in Biteau et al. (2020), it is possible to distinguish three kind of extreme behaviours: HBL sources showing extreme behaviour during flaring states, when synchrotron and IC peaks shift towards higher frequencies, going back to their standard HBL-like state, as observed for Mrk501 (Ghisellini 1999); sources with a steady hard synchrotron without evidence for a hard spectrum at TeV energies; finally, sources showing a persistently hard IC hump peaking at and above TeV energies and a synchrotron peak in the X-ray band. Our excellent X-ray and VHE gamma-ray data allowed us to search for these signatures in the SEDs that we measured at different times for TXS 1515–273.

TXS 1515–273 was very little studied before the flare occurred in 2019. As explained in the previous sections, the photon index reported by Abdollahi et al. (2020) seemed to suggest a possible EHBL classification. Thus, we examined archival data from the ASI

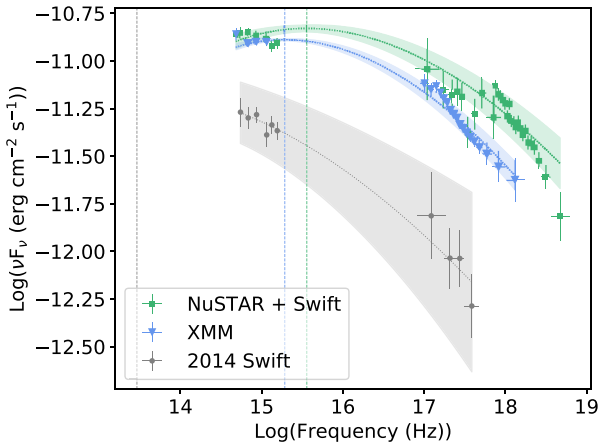

Figure 6. Results of the fit of the SED synchrotron bump with a log-parabola. Data are shown in different colours, representing: *NuSTAR* epoch (*NuSTAR* and *Swift* data sets taken on MJD 58544.84 and 58544.97, green squares), *XMM* epoch (*XMM–Newton* and *XMM-OM* data set, blue triangles), 2014 *Swift* data set (grey circles). Dotted curves are showed superimposed on SED points with the same colours, representing the fit curves and the uncertainty bands. Vertical dashed line are also shown, in correspondence of the peak frequency evaluated from the fit parameters.

Table 4. Results of the log-parabola fit of the synchrotron peak of the SED of the three different epochs considered.

Epoch	Log of peak frequency (Hz)
2014 *Swift*	13.46 ± 2.53
XMM	15.28 ± 0.06
NuSTAR and 2019 *Swift*	15.56 ± 0.11

Space Science Data Center (SSDC)[9] to test if the source could indeed be classified as such. According to Bonnoli et al. (2015), a good criterion to select EHBLs relies on the high X-ray-to-radio flux ratio. As reported by the authors, a high ratio of X-ray versus radio flux ($F_X/F_R > 10^4$) would indicate a good EHBL candidate. Based on archival data, considering the flux in the $\sim 10^{16}$–10^{19} Hz band and in the $\sim 10^{9}$–10^{10} Hz band for F_X and F_R, respectively, we found a ratio of ∼30, which led us to the conclusion that it was not a good EHBL candidate.

In order to estimate the peak frequency and classify the source, we combined strictly simultaneous data in the optical and X-ray band to perform a fit of a log-parabola to the data in the log–log plane:

$$\nu F_\nu(\nu) = f_0\, 10^{-b\ (\log_{10}(\nu/\nu_s))^2}, \quad (5)$$

where ν_s is the peak frequency. This fit was performed separately on data from the current observations and a previous *Swift*-UVOT and *Swift*-XRT observations from 2014. We considered data from the two epochs separately in order to take into account a possible shift in the peak frequency between the two observing periods, combining *Swift*-XRT observations from MJD 58544.84 and 58544.97 with the *NuSTAR* data set. The results of the fit procedure on the three considered data sets are reported in Fig. 6. The best-fitting values for the three data sets are reported in Table 4.

The best-fitting values found for the most recent observations classify the source as HSP during the flare. For 2014 data, however, the value found $\nu_s \simeq 10^{13.46 \pm 2.53}$ Hz does not allow any conclusion to be drawn on the classification of the source. However, it is clear that ν_s moved to higher energy between the *XMM–Newton* and the *NuSTAR* observations, which were separated by less than a day. This is most naturally explained by the injection of fresh electrons or the dominance of a new emission component. Even in the flaring state detected by *NuSTAR* the peak frequency does not exceed 10^{17} and therefore it is clear that TXS 1515–273 is not an extreme synchrotron peaked source.

[9] http://www.asdc.asi.it/

5.2 Emission models

Most blazars' observations are fitted with radiative models. These models are usually classified as leptonic and hadronic models.

In the simple one-zone SSC model, TeV emission is the result of the IC scattering of electrons and positrons in the jet on photons created by the electron population itself via synchrotron emission. The SSC model is supported by several observations of good temporal correlation between the TeV and X-ray flares (see Coppi & Aharonian 1999; Maraschi et al. 1999; Takahashi et al. 2000; Krawczynski et al. 2001). In this simple one-zone SSC model, the energy density has been found to be largely dominated by particle energy density rather than the magnetic field; this unusually low magnetization seems to be in contradiction with theoretical and observational constraints of equipartition conditions, which cannot be reproduced in BL Lac objects with the one-zone model (Tavecchio & Ghisellini 2016). It was recently suggested, however, that equipartition can be achieved in one-zone models via the introduction of an anisotropic electron population (Tavecchio & Sobacchi 2020). The one-zone SSC is still the default model and, given the fact that during this campaign all of the energy bands were found to be in the same high state, we apply this model to the data using the constraints for the size of the emission region and magnetic field strength we found in Section 4.3.

Another possible way to solve the contradiction on the low magnetization can be obtained by taking into consideration the existence of additional seed photons from other parts of the jet (e.g. Georganopoulos & Kazanas 2003; Ghisellini, Tavecchio & Chiaberge 2005). In these models, one assumes the jet to be structured. As shown in Tavecchio & Ghisellini (2015), the assumption of a supplementary source of soft photons intervening in the IC emission allows the reproduction of the observed SED assuming equipartition between the magnetic and the electron energy densities. There is also observational evidence for spine-sheath models from very long baseline interferometry observations (e.g. Attridge, Roberts & Wardle 1999; Giroletti et al. 2004) and indications for multiple components contributing to the optical band from long-term variability (Lindfors et al. 2016) and polarization (see e.g. Valtaoja et al. 1991).

In our case, the X-ray variability indicates that the X-ray emission region is very compact. Therefore, it must either be located very close to the central engine (to fill the full diameter of the conical jet) or be embedded in a larger emission region. Our X-ray light curves show several flares and the SED peak moves to higher energies from the *XMM–Newton* epoch to the *NuSTAR* epoch. This can be either due to the variation of the particle distributions within the emission region (e.g. fresh injection of particles) or due to the flaring region (filling the full diameter of the jet) consisting of several emission regions. Therefore, we also model the SEDs with a two-component model such that we keep the parameters of the larger region constant between the two SED epochs and only vary the parameters of the small emission region.

Another possible explanation of the VHE emission observed is given by hadronic models (e.g. Mannheim 1993; Mücke & Protheroe 2001; Aharonian & Taylor 2010; Cerruti et al. 2015), where energetic

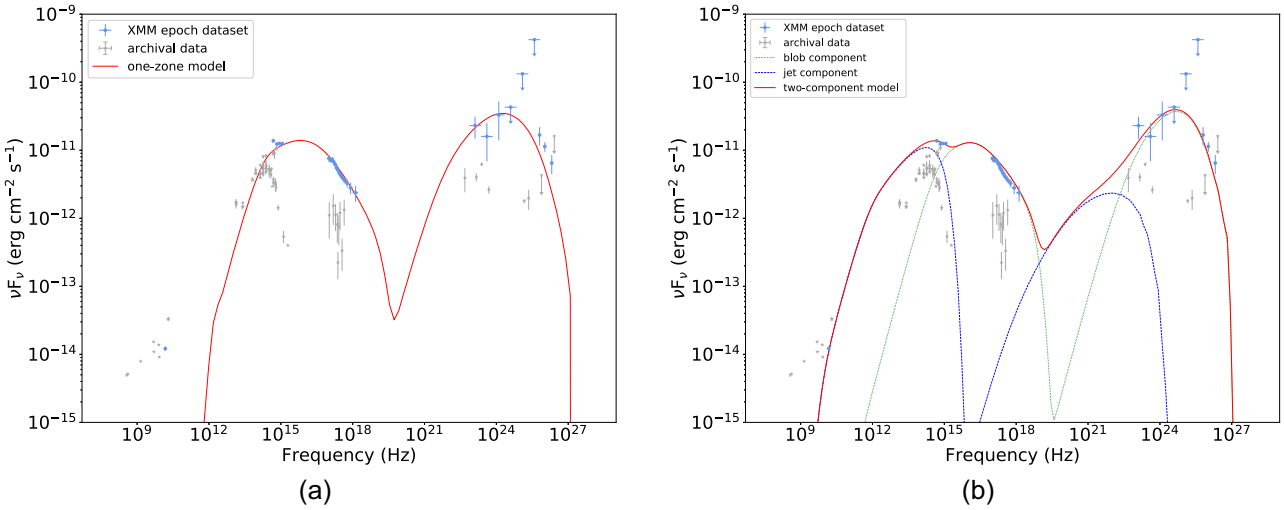

Figure 7. Broad-band SED and modelled spectra for TXS 1515–273. The SED has been modelled considering the VLBA SED point in the radio band, KVA, *XMM-OM*, and *XMM–Newton* SED points in the optical and X-ray energy band and the *Fermi*-LAT and MAGIC SED points in the gamma-ray band, using a one-zone model (left) and a two-component model (right). Coloured points represent observations in the different energy bands during the observations of 2019, grey points represent archival data. The red solid line represents the models, the green dotted line represents the blob emission and the blue dashed line represents the jet emission. Further details can be found in the text. See Table 5 for parameters.

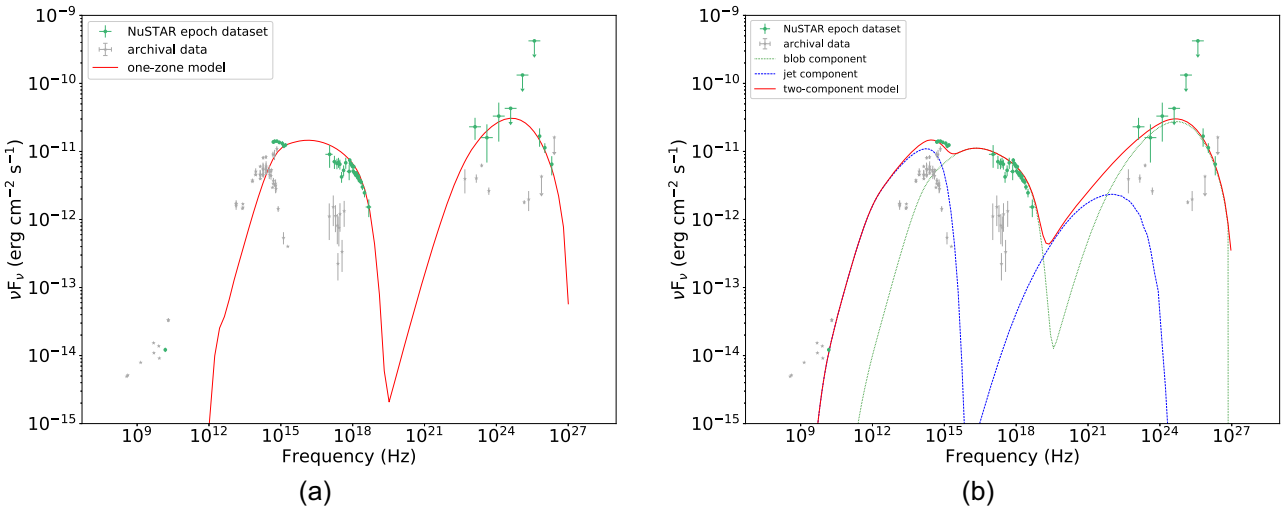

Figure 8. Broad-band SED and modelled spectra for TXS 1515–273. The SED has been modelled considering the VLBA SED point in the radio band, KVA, *Swift*, and *NuSTAR* SED points in the optical and X-ray energy band and the *Fermi*-LAT and MAGIC SED points in the gamma-ray band, using a one-zone model (left) and a two-component model (right). Only *Swift* data simultaneous to *NuSTAR* observations were used. Coloured points represent observations in the different energy bands during the observations of 2019, grey points represent archival data. The red solid line represents the models, the green dotted line represents the blob emission and the blue dashed line represents the jet emission. Further details can be found in the text. For parameters, see Table 5.

photons are produced in jets via hadronic interactions. These models are based on the assumption of the presence of high-energy protons in the jet which are accelerated together with the electrons. While the low-energy peak is still explained by synchrotron radiation of electrons, in this scenario the VHE gamma-rays are thought to be produced by interactions of the relativistic protons with soft photons or with the magnetic field. In particular, the recent indication of a link between a neutrino track event and the blazar TXS 0506+056 (Aartsen et al. 2018a, b) can be interpreted in a lepto-hadronic scenario where electrons and protons are accelerated in the jet, and synchrotron photons from the electrons lead to photo-hadronic neutrino production (Ansoldi et al. 2018; Keivani et al. 2018; Cerruti et al. 2019).

However, since our study shows that TXS 1515–273 is a rather typical HSP in flaring state and since no neutrinos have been detected from the direction of TXS 1515–273 (Aartsen et al. 2020), in the next section we investigate only one-zone and two-component leptonic models for the SED.

5.3 Spectral energy distribution modelling

We derived the broad-band SED from radio to VHE shown in Figs 7 and 8. For comparison purposes, archival data from the SSDC and from a previous *Swift*-XRT detection are also shown as grey dots.

The light curve in the *Fermi*-LAT band showed the presence of a high-flux state on MJD 58546. Since no VHE observations

Table 5. SED modelling parameters for one-zone SSC and two-component models. Parameters are reported for the two available X-ray data set. See the text for the description of the parameters and the models.

X-ray data set	Model	Component	$\gamma_{\rm min}$ ($\times 10^3$)	$\gamma_{\rm b}$ ($\times 10^4$)	$\gamma_{\rm max}$ ($\times 10^5$)	n_1	n_2	B (G)	K ($\times 10^4$ cm^{-3})	R ($\times 10^{15}$ cm)	δ	$U_{\rm B}/U_{\rm E}$
XMM–Newton	one-zone	–	4.3	3.1	10.0	2.21	3.95	0.14	59	4.56	18	5×10^{-3}
	2-component	blob	6.0	3.5	6.0	1.96	4.0	0.14	6.1	3.95	18	4×10^{-3}
		jet	0.52	0.52	0.19	1.74	2.84	0.14	0.0041	320	3.8	1.4
NuSTAR	one-zone	–	4.9	5	4.5	2.51	3.72	0.14	980	3.22	24	6×10^{-3}
	2-component	blob	2.5	2.7	5.8	1.99	3.5	0.14	9.3	2.92	22	3×10^{-3}
		jet	0.52	0.52	0.19	1.74	2.84	0.14	0.0041	320	3.8	1.4

were available on that day, we performed the *Fermi*-LAT spectral analysis starting from MJD 58541 up to MJD 58545 in order to have a smooth connection between the HE and the VHE gamma-ray observations. For what concerns the optical and X-ray observations, since these were not simultaneous and the source showed short-term variability in the X-ray energy range, we decided to separate the data sets into *NuSTAR*, *Swift*-XRT, and *Swift*-UVOT observations and *XMM–Newton* and *XMM-OM* observations. We modelled these data sets separately since the model we adopted is not time dependent.

Given the fact that the source was in a high state in all energy bands, the SED was at first modelled with a simple one-zone SSC model; the radiation is emitted in a region in the jet by a single homogeneous population of electrons (Maraschi & Tavecchio 2003) which is responsible for the emission from infrared to VHE frequencies. The emitting region can be described as a sphere with radius R with a uniform magnetic field B. The Doppler factor, δ, is required to take into account the relativistic effects. For HSP sources, this factor is usually ∼10–50: within this range we selected a value for each epoch that would reproduce a model in good agreement with our data, having a consistent model by using the same value of δ to estimate R and B.

A good agreement between the model and the SED data was found using $\delta = 18$ for the *XMM–Newton* epoch, which corresponds to an estimated magnetic field intensity $B = 0.14 \pm 0.02$ G and to an upper limit on the size equal to $R \leq 4.56 \pm 0.83 \times 10^{15}$ cm, and $\delta = 24$ for the *NuSTAR* epoch, which corresponds to $B = 0.13 \pm 0.02$ G and $R \leq 3.28 \pm 0.69 \times 10^{15}$ cm.

The population of relativistic electrons is described by a broken power-law model, where K is a normalization factor that represents the density of electrons with $\gamma = 1$, n_1 the index from $\gamma_{\rm min}$ to $\gamma_{\rm br}$ and n_2 from $\gamma_{\rm br}$ to $\gamma_{\rm max}$, for a total of six parameters. The model includes the Klein–Nishina cross-section $\sigma_{\rm KN}$ for the IC spectrum calculation, which is important in the case of emission above the GeV range. Since our analyses in Sections 4.2 and 5.1 clearly demonstrated that between the *XMM–Newton* and *NuSTAR* observing epochs the synchrotron peak moved to higher energies and spectral evolution with time changed the pattern, we assume that the new blob dominates the emission in the *NuSTAR* epoch, i.e. we let the electron energy spectrum parameters vary rather arbitrarily between the two epochs.

For both data sets, we found acceptable agreement between the models and the data available from optical to VHE gamma-ray (see Figs 7a and 8a). The parameters of the one-zone model are given in Table 5. Even if we tried a large number of different combinations of parameters, it was hard to find parameters that would reproduce well the shape of the synchrotron bump. Parameters that would describe well the shape of the spectrum in the X-ray band led to an underestimation of the optical flux while changing the set of parameters so that the optical shape was well described by the model would overproduce the X-ray flux. Moreover, we also had to take into account the IC bump which extends to VHE gamma-ray energies. In the *XMM–Newton* epoch, the biggest challenge for the model is to reproduce the rather soft *XMM–Newton* spectra and still let the second peak extend to VHE gamma-rays without overproducing the HE gamma-ray part. The selected model is a compromise and is below the VHE gamma-ray points. In the *NuSTAR* epoch, the selected model produces well the level of the flux in the UV-band and the shape and level of the *NuSTAR* observations, but does not describe the shape in the optical band and overproduces the *Swift*-XRT data. The second bump is well described in the *NuSTAR* epoch.

As expected, the one-zone model is not able to reproduce the emission at radio frequencies (15 GHz): this is due to the small and dense emission region. The emission foreseen by the one-zone model is synchrotron self-absorbed. It is likely that the radio flux originates from a different, larger, region of the jet, transparent at those frequencies. Also, as is typical for one-zone models, both the *XMM–Newton* and *NuSTAR* one-zone models are far from equipartition (see Table 5, last column).

The two-component model could potentially improve the modelling of the synchrotron component and there exists numerous observational evidence supporting two-component models for BL Lac objects in general (see Section 5.2). Therefore, we modelled the observed SEDs with the two-component model described in MAGIC Collaboration (2020b), and references therein. The model includes two spherical blobs embedded in one another which are interacting. Each of the blobs is filled with relativistic electrons with a broken power-law distribution. The two blobs have the same magnetic field strength, but different Doppler factors and sizes, increasing the number of parameters from eight to 15. We call the two emission regions 'blob' (smaller region) and 'jet' (larger region). The interaction between the emission regions provides additional seed photons for Compton scattering. The larger emission region dominantly provides seed photons to the smaller region (Tavecchio et al. 2011). The gamma–gamma absorption is negligible (see MAGIC Collaboration 2020b). The two-component model describes the data from the radio to the VHE range well (see Figs 7b and 8b) with the parameters given in Table 5. The improvement with respect to the one-zone model is most evident in the radio and optical part. While the lowest radio frequencies are still not reproduced in the two-component model, the 'jet' component connects smoothly the 15 GHz MOJAVE point to the optical data and the shape of the optical SED is reproduced better. The jet component is closer to equipartition, but we do not find solutions where the blob component itself would be in equipartition; indeed, for *XMM–Newton* and *NuSTAR* we find values of the order of

10^{-3}–10^{-4}. The main difficulty is to produce the Compton dominance we see in the observed SED.

6 SUMMARY AND DISCUSSION

In this paper, we present an MWL analysis of the source TXS 1515–273, a BL Lac object which had been very little studied before this campaign. When compared to archival data in the X-ray and HE gamma-ray energy bands and optical monitoring following the analysed period, at the end of 2019 February the source was found to be in a flaring state in all energy bands, which lead to its first detection in the VHE gamma-ray band by MAGIC. Since this time, no further TeV observations have been published so no additional information on its VHE gamma-ray emission is available.

Thanks to the very good X-ray coverage of the source during the flaring state it was possible to detect an hour-scale variability in the X-ray fluxes and a clear change in the spectral shape between the *XMM–Newton* (MJD 58544) and *NuSTAR* (MJD 58545) observations. We produced the *XMM–Newton* and *NuSTAR* light curves in two energy bins each and constrained the rise and decay times of the flares. We find rapid variations on the time-scale of the order of hours in both data sets. Studies of variability of blazars in the *NuSTAR* band (Bhatta, Mohorian & Bilinsky 2018) show that the time-scale we found is in line with the fastest variability seen in many HSP sources. In few cases, even shorter time-scales variability has been found, e.g. for Mrk 421 (MAGIC Collaboration 2020a) and for 1ES 1959+650 (MAGIC Collaboration 2020c), although different analytical functions were adopted in these works to profile the flares. The short time-scale variability was used to constrain the size of the emission region and the intensity of the magnetic field, both used later during the analysis to find a suitable model for the broad-band emission.

TXS 1515–273 was very little studied prior to this work and therefore the source had not yet been properly classified. Up to and including the 3FGL *Fermi*-LAT catalogue, the source was still classified as a blazar candidate of uncertain type. Only in the 4FGL catalogue was it classified as a BL Lac object, but the SED type was not defined. The good coverage in the optical–X-ray energy band obtained in this observational campaign allowed an accurate determination of the synchrotron peak frequency ν_s and the classification of the source as a HSP source during this flare. Furthermore, during the flare, the peak clearly shifted to higher energies in a time-scale of less than a day. Such behaviour is rather common in blazars, see e.g. Pian et al. (1998) or MAGIC Collaboration (2020c), in which a clear shift in the synchrotron bump was reported during flare activity with respect to archival data. In our case, thanks to very good X-ray coverage we could follow this shift on daily time-scales.

We also investigated the behaviour of the jet at 15 GHz using the VLBA data from the MOJAVE program. We found no new components or moving components, which is in line with what is seen in other TeV blazars with high synchrotron peak frequency (see e.g. Piner & Edwards 2018, and references therein). HSP objects usually do not show high linear core polarization levels (Lister et al. 2011), which is what we also find for TXS 1515-273 in the first epochs of data. However, in 2019 the core was significantly polarized, which might be connected to the general high state, but the sparse coverage of the VLBA observations did not allow a strong conclusion to be drawn.

We also modelled the broad-band SED from radio to VHE gamma-rays. The evolution of the SED from the *XMM–Newton* to the *NuSTAR* epoch clearly suggests that an injection of new electrons or a new blob is starting to dominate the emission. The one-zone model describes well the data from the X-ray band to VHE gamma-rays for both epochs, but has problems reproducing the shape of the optical part of the SED and does not reproduce the radio. The latter is expected as the small emitting region considered is optically thick to radio emission. The radio emission must then originate from a different component. These issues are solved when a two-component model is considered, in which the blob is responsible for the emission from X-ray to VHE gamma-rays, while the jet dominates the emission at radio wavelengths. The introduction of the two-component model increases the number of model parameters from eight to 15, allowing for a more accurate modelling of the emission. In particular, the jet emission results in important contributions in the optical band. Moreover, assuming the two emission regions to be co-spatial, seed photons for the IC scattering are provided also from the jet.

Finally, we examined the ratio between the magnetic field density and the electron energy density, U_B/U_E. In both epochs, we find that the one-zone SED parameters are quite far from equipartition, with the magnetic field energy density dominated by the kinetic energy of the relativistic particles by several orders of magnitude. In the two-component model instead the jet itself is in equipartition, but within the constraints on emission region size and magnetic field strength we derived from the X-ray observations (assuming 'typical' Doppler factors), we did not find solutions where the blob would be in equipartition. We note that Tavecchio & Ghisellini (2016) found a two-component model solution for the low-state SED of Mrk421 where the blob itself was in equipartition. However, this seems not to always be possible in the case of flares (see also MAGIC Collaboration 2019).

ACKNOWLEDGEMENTS

We would like to thank the Instituto de Astrofísica de Canarias for the excellent working conditions at the Observatorio del Roque de los Muchachos in La Palma. The financial support of the German BMBF, MPG, and HGF; the Italian INFN and INAF; the Swiss National Fund SNF; the ERDF under the Spanish Ministerio de Ciencia e Innovación (MICINN) (FPA2017-87859-P, FPA2017-85668-P, FPA2017-82729-C6-5-R, FPA2017-90566-REDC, PID2019-104114RB-C31, PID2019-104114RB-C32, PID2019-105510GB-C31, PID2019-107847RB-C41, PID2019-107847RB-C42, PID2019-107847RB-C44, PID2019-107988GB-C22); the Indian Department of Atomic Energy; the Japanese ICRR, the University of Tokyo, JSPS, and MEXT; the Bulgarian Ministry of Education and Science, National RI Roadmap Project DO1-268/16.12.2019 and the Academy of Finland grant nr. 317637 and 320045 are gratefully acknowledged. This work was also supported by the Spanish Centro de Excelencia 'Severo Ochoa' SEV-2016-0588, SEV-2017-0709 and CEX2019-000920-S, and 'María de Maeztu' CEX2019-000918-M, the Unidad de Excelencia 'María de Maeztu' MDM-2015-0509-18-2 and the 'la Caixa' Foundation (fellowship LCF/BQ/PI18/11630012), by the Croatian Science Foundation (HrZZ) Project IP-2016-06-9782 and the University of Rijeka Project 13.12.1.3.02, by the DFG Collaborative Research Centers SFB823/C4 and SFB876/C3, the Polish National Research Centre grant UMO-2016/22/M/ST9/00382 and by the Brazilian MCTIC, CNPq, and FAPERJ.

The *Fermi*-LAT Collaboration acknowledges generous ongoing support from a number of agencies and institutes that have supported both the development and the operation of the LAT as well as

scientific data analysis. These include the National Aeronautics and Space Administration and the Department of Energy in the United States, the Commissariat à l'Energie Atomique and the Centre National de la Recherche Scientifique/Institut National de Physique Nucléaire et de Physique des Particules in France, the Agenzia Spaziale Italiana and the Istituto Nazionale di Fisica Nucleare in Italy, the Ministry of Education, Culture, Sports, Science and Technology (MEXT), High Energy Accelerator Research Organization (KEK) and Japan Aerospace Exploration Agency (JAXA) in Japan, and the K. A. Wallenberg Foundation, the Swedish Research Council and the Swedish National Space Board in Sweden. Additional support for science analysis during the operations phase from the following agencies is also gratefully acknowledged: the Istituto Nazionale di Astrofisica in Italy and the Centre National d'Etudes Spatiales in France.

This research has made use of data and/or software provided by the High Energy Astrophysics Science Archive Research Center (HEASARC), which is a service of the Astrophysics Science Division at NASA/GSFC. This research has made use of data from the MOJAVE data base that is maintained by the MOJAVE team (Lister et al. 2018).

DATA AVAILABILITY

The data underlying this article will be shared on reasonable request to the corresponding author.

REFERENCES

Aartsen M. G. et al., 2018a, Science, 361, 147
Aartsen M. G. et al., 2018b, Science, 361, eaat1378
Aartsen M. G. et al., 2020, Phys. Rev. Lett., 124, 051103
Abdo A. A. et al., 2010, ApJ, 716, 30
Abdollahi S. et al., 2020, ApJS, 247, 33
Acero F. et al., 2015, ApJS, 218, 23
Acero F. et al., 2016, ApJS, 223, 26
Ackermann M. et al., 2011, ApJ, 743, 171
Ackermann M. et al., 2013, ApJS, 209, 34
Ackermann M. et al., 2015, ApJ, 810, 14
Ackermann M. et al., 2016, ApJS, 222, 5
Aharonian F., 2000, New Astron., 5, 377
Aharonian F., Taylor A. M., 2010, Astropart. Phys., 34, 258
Ahnen M. et al., 2017, Astropart. Phys., 94, 29
Ajello M. et al., 2017, ApJS, 232, 18
Aleksić J. et al., 2016, Astropart. Phys., 72, 76
Ansoldi S. et al., 2018, ApJ, 863, L10
Attridge J. M., Roberts D. H., Wardle J. F. C., 1999, ApJ, 518, L87
Atwood W. B. et al., 2009, ApJ, 697, 1071
Barthelmy S. D. et al., 2005, Space Sci. Rev., 120, 143
Becerra González J., Acosta-Pulido J. A., Boschin W., Clavero R., Otero-Santos J., Carballo-Bello J. A., Domínguez-Palmero L., 2021, MNRAS, 504, 5258
Bertero M., 1989, Linear Inverse and III-Posed Problems. Academic Press, New York, p. 1
Bhatta G., Mohorian M., Bilinsky I., 2018, A&A, 619, A93
Biteau J. et al., 2020, Nat. Astron., 4, 124
Bonnoli G., Tavecchio F., Ghisellini G., Sbarrato T., 2015, MNRAS, 451, 611
Breeveld A. A. et al., 2010, MNRAS, 406, 1687
Burrows D. N. et al., 2005, Space Sci. Rev., 120, 165
Cardelli J. A., Clayton G. C., Mathis J. S., 1989, ApJ, 345, 245
Cerruti M., Zech A., Boisson C., Inoue S., 2015, MNRAS, 448, 910
Cerruti M., Zech A., Boisson C., Emery G., Inoue S., Lenain J. P., 2019, MNRAS, 483, L12
Coppi P. S., Aharonian F. A., 1999, ApJ, 521, L33
Costamante L., Ghisellini G., 2002, A&A, 384, 56
Costamante L. et al., 2001, A&A, 371, 512
Cutini S., 2019, Astron. Telegram, 12532, 1
Den Herder J. W. et al., 2001, A&A, 365, L7
Domínguez A. et al., 2011, MNRAS, 410, 2556
Evans P. A. et al., 2009, MNRAS, 397, 1177
Fallah Ramazani V., Lindfors E., Nilsson K., 2017, A&A, 608, A68
Foffano L., Prandini E., Franceschini A., Paiano S., 2019, MNRAS, 486, 1741
Fossati G., Maraschi L., Celotti A., Comastri A., Ghisellini G., 1998, MNRAS, 299, 433
Fukugita M., Shimasaku K., Ichikawa T., 1995, PASP, 107, 945
Gehrels N. et al., 2004, ApJ, 611, 1005
Georganopoulos M., Kazanas D., 2003, ApJ, 594, L27
Ghisellini G., 1999, Astropart. Phys., 11, 11
Ghisellini G., Tavecchio F., Chiaberge M., 2005, A&A, 432, 401
Ghisellini G., Righi C., Costamante L., Tavecchio F., 2017, MNRAS, 469, 255
Giroletti M. et al., 2004, ApJ, 600, 127
Goldoni P. et al., 2021, A&A, 650, A106
Harrison F. A. et al., 2013, ApJ, 770, 103
Jansen F. et al., 2001, A&A, 365, L1
Kaur A., Rau A., Ajello M., Domínguez A., Paliya V. S., Greiner J., Hartmann D. H., Schady P., 2018, ApJ, 859, 80
Keenan M., Meyer E. T., Georganopoulos M., Reddy K., French O. J., 2021, MNRAS, 505, 4726
Keivani A. et al., 2018, ApJ, 864, 84
Kirk J. G., Rieger F. M., Mastichiadis A., 1998, A&A, 333, 452
Krawczynski H. et al., 2001, ApJ, 559, 187
Lefaucheur J., Pita S., 2017, A&A, 602, A86
Lindfors E. J. et al., 2016, A&A, 593, A98
Lister M. L. et al., 2011, ApJ, 742, 27
Lister M. L., Aller M. F., Aller H. D., Hodge M. A., Homan D. C., Kovalev Y. Y., Pushkarev A. B., Savolainen T., 2018, ApJS, 234, 12
Lister M. L. et al., 2019, ApJ, 874, 43
MAGIC Collaboration, 2019, A&A, 623, A175
MAGIC Collaboration, 2020a, ApJS, 248, 29
MAGIC Collaboration, 2020b, A&A, 640, A132
MAGIC Collaboration, 2020c, A&A, 638, A14
Mannheim K., 1993, A&A, 269, 67
Maraschi L., Tavecchio F., 2003, ApJ, 593, 667
Maraschi L. et al., 1999, ApJ, 526, L81
Mirzoyan R., 2019, Astron. Telegram, 12538, 1
Mücke A., Protheroe R. J., 2001, Astropart. Phys., 15, 121
Murase K., Dermer C. D., Takami H., Migliori G., 2012, ApJ, 749, 63
Nilsson K. et al., 2018, A&A, 620, A185
Nolan P. L. et al., 2012, ApJS, 199, 31
Oh K. et al., 2018, ApJS, 235, 4
Padovani P. et al., 2017, A&AR, 25, 2
Pian E. et al., 1998, ApJ, 492, L17
Piner B. G., Edwards P. G., 2018, ApJ, 853, 68
Poole T. S. et al., 2008, MNRAS, 383, 627
Roming P. W. A. et al., 2005, Space Sci. Rev., 120, 95
Schlafly E. F., Finkbeiner D. P., 2011, ApJ, 737, 103
Stickel M., Padovani P., Urry C. M., Fried J. W., Kuehr H., 1991, ApJ, 374, 431
Stocke J. T., Morris S. L., Gioia I. M., Maccacaro T., Schild R., Wolter A., Fleming T. A., Henry J. P., 1991, ApJS, 76, 813
Strüder L. et al., 2001, A&A, 365, L18
Takahashi T. et al., 2000, ApJ, 542, L105
Tavecchio F., Ghisellini G., 2015, MNRAS, 456, 2374
Tavecchio F., Ghisellini G., 2016, MNRAS, 456, 2374
Tavecchio F., Sobacchi E., 2020, MNRAS, 491, 2198
Tavecchio F., Ghisellini G., Ghirlanda G., Foschini L., Maraschi L., 2010, MNRAS, 401, 1570
Tavecchio F., Becerra-Gonzalez J., Ghisellini G., Stamerra A., Bonnoli G., Foschini L., Maraschi L., 2011, A&A, 534, A86

Turner M. J. L. et al., 2001, A&A, 365, L27
Valtaoja L., Sillanpaa A., Valtaoja E., Shakhovskoi N. M., Efimov I. S., 1991, AJ, 101, 78
Wachter K., Leach R., Kellogg E., 1979, ApJ, 230, 274
Willingale R., Starling R. L. C., Beardmore A. P., Tanvir N. R., O'Brien P. T., 2013, MNRAS, 431, 394
Zanin R. et al., 2013, in International Cosmic Ray Conference, 33, 2937
Zhang Y. et al., 2002, ApJ, 572, 762

APPENDIX A: DETAILS OF THE MULTIWAVELENGTH ANALYSIS

Here, we provide more detail on the observations and the analysis performed in the different energy ranges.

Table A1. Observed flux of TXS 1515–273 observation with MAGIC. The 95 per cent confidence level upper limits are also reported for observations with less than 3σ significance.

MJD	Time (h)	Flux (> 400 GeV) ($\times 10^{-12}$ cm^{-2} s^{-1})	Flux (> 400 GeV) UL ($\times 10^{-12}$ cm^{-2} s^{-1})	Significance σ
58541.21	1.31	6.28 ± 2.16		3
58542.27	1.97	7.42 ± 1.29		7
58543.20	1.31	–	4.47	0
58544.19	0.35	–	1.79	0.7
58545.22	2.12	3.85 ± 1.19		5
58547.19	1.04	–	4.65	1

Table A2. Observed flux of TXS 1515–273 observation with *Fermi*-LAT. The exposure time for each bin is 24 h, and the MJD values reported in the first column correspond to the middle of the time bin. The 95 per cent confidence level upper limits are reported for bins with TS < 9.

MJD	Flux (> 300 MeV) ($\times 10^{-7}$ cm^{-2} s^{-1})	Flux (> 300 MeV) UL ($\times 10^{-7}$ cm^{-2} s^{-1})	TS
58539.22	0.635 ± 0.328		9.36
58540.22	0.821 ± 0.371		11.75
58541.22	0.674 ± 0.316		22.00
58542.22	0.549 ± 0.296		11.35
58543.22	–	0.228	0
58544.22	0.511 ± 0.294		10.62
58545.22	–	1.266	6.74
58546.22	4.664 ± 0.842		138.29
58547.22	–	0.192	0
58548.22	–	1.020	0.97

Table A3. Log and fitting results of *XMM–Newton* observations of TXS 1515–273 with $N_{\rm H}$ fixed to Galactic absorption. Fluxes are corrected for the Galactic absorption.

MJD	Exposure time (ks)	Flux (3–10 keV) ($\times 10^{-12}$ erg cm^{-2} s^{-1})	Flux (0.3–10 keV) ($\times 10^{-12}$ erg cm^{-2} s^{-1})
58544.10	25	2.47 ± 0.02	8.16 ± 0.05

Table A4. Log and fitting results of *NuSTAR* observations of TXS 1515–273 with $N_{\rm H}$ fixed to Galactic absorption. Fluxes are corrected for the Galactic absorption.

MJD	Exposure time (ks)	Flux (3–10 keV) ($\times 10^{-12}$ erg cm^{-2} s^{-1})	Flux (4–79 keV) ($\times 10^{-12}$ erg cm^{-2} s^{-1})
58544.95	34	5.69 ± 0.04	3.25 ± 0.02

Table A5. Log and fitting results of *Swift*-XRT observations of TXS 1515–273 using a PL model with N_H fixed to Galactic absorption. Fluxes are corrected for the Galactic absorption.

MJD	Exposure time (s)	Flux 0.3–10 keV ($\times 10^{-12}$ erg cm^{-2} s^{-1})	Photon index (Γ_X)
56930.87	1193.7	1.08 ± 0.20	2.84 ± 0.32
58488.34	229.8	5.37 ± 0.11	2.55 ± 0.30
58541.65	2462.3	1.69 ± 0.65	2.14 ± 0.51
58544.12	536.6	8.16 ± 0.81	2.50 ± 0.14
58544.84	401.2	1.78 ± 0.21	2.00 ± 0.15
58544.97	529.0	1.75 ± 0.19	2.29 ± 0.15
58547.43	2497.3	3.83 ± 0.23	2.73 ± 0.10
58551.62	1648.2	2.73 ± 0.26	2.89 ± 0.14
58554.60	2582.2	5.24 ± 0.29	2.61 ± 0.92
58560.71	2467.3	2.38 ± 0.17	2.88 ± 0.13

Table A6. Observed magnitudes with *XMM-OM*.

MJD	B (AB mag)	U (AB mag)	W1 (AB mag)
58544.10	16.639 ± 0.005	17.089 ± 0.008	17.406 ± 0.009

Table A7. Observed magnitudes for TXS 1515–273 with Siena Observatory.

MJD	Observed magnitude (mag)
58542.17	15.43 ± 0.02
58551.14	15.50 ± 0.02
58564.10	15.56 ± 0.03

Table A8. Observed magnitudes with KVA.

MJD	Observed magnitude (mag)
58541.22	15.46 ± 0.02
58542.21	15.42 ± 0.02
58543.23	15.5 ± 0.02
58544.24	15.43 ± 0.06
58545.24	15.44 ± 0.02
58547.23	15.39 ± 0.02
58549.24	15.45 ± 0.02
58551.22	15.48 ± 0.02
58552.24	15.54 ± 0.02
58554.21	15.48 ± 0.02
58555.2	15.39 ± 0.02
58556.2	15.46 ± 0.02
58557.19	15.51 ± 0.02
58558.17	15.52 ± 0.02
58559.24	15.57 ± 0.02
58560.22	15.66 ± 0.08
58565.25	15.68 ± 0.03
58580.18	15.78 ± 0.02
58584.2	15.8 ± 0.03
58586.19	15.76 ± 0.02
58596.14	15.99 ± 0.04
58600.16	15.92 ± 0.03
58603.14	15.93 ± 0.03
58609.95	16.0 ± 0.06
58617.12	16.05 ± 0.04
58633.9	15.89 ± 0.03
58643.93	16.11 ± 0.03
58658.97	16.14 ± 0.03
58666.94	16.14 ± 0.03

Table A8 – *continued*

MJD	Observed magnitude (mag)
58673.92	16.0 ± 0.03
58678.91	16.08 ± 0.04
58687.9	15.95 ± 0.03
58692.91	15.98 ± 0.03
58699.92	16.03 ± 0.03
58706.89	16.0 ± 0.04
58714.88	15.93 ± 0.03
58718.87	15.86 ± 0.03

Table A9. Observed magnitudes for TXS 1515–273 obtained with *Swift*-UVOT.

MJD	V (mag)	B (mag)	U (mag)	W1 (mag)	M2 (mag)	W2 (mag)
56930	16.74 ± 0.14	17.72 ± 0.16	16.96 ± 0.12	17.50 ± 0.16	17.71 ± 0.14	17.74 ± 0.12
58488	–	–	16.58 ± 0.07	–	–	–
58541	15.95 ± 0.06	16.56 ± 0.06	15.97 ± 0.06	16.19 ± 0.07	16.60 ± 0.09	16.52 ± 0.07
58544	15.89 ± 0.07	16.60 ± 0.06	15.92 ± 0.07	16.23 ± 0.08	16.67 ± 0.10	16.58 ± 0.07
58547	15.87 ± 0.05	16.49 ± 0.05	15.88 ± 0.06	16.25 ± 0.07	16.58 ± 0.08	16.60 ± 0.07
58551	16.07 ± 0.07	16.59 ± 0.06	16.01 ± 0.07	16.36 ± 0.08	16.70 ± 0.09	16.63 ± 0.08
58554	15.87 ± 0.05	16.52 ± 0.05	15.82 ± 0.06	16.24 ± 0.07	16.50 ± 0.08	16.52 ± 0.07
58560	16.09 ± 0.06	16.77 ± 0.06	16.10 ± 0.06	16.37 ± 0.08	16.70 ± 0.08	16.84 ± 0.07

[1]*Inst. de Astrofísica de Canarias and Dpto. Astrofísica, Universidad de La Laguna, E-38200 La Laguna, Tenerife, Spain*
[2]*Università di Udine and INFN Trieste, I-33100 Udine, Italy*
[3]*National Institute for Astrophysics (INAF), I-00136 Rome, Italy*
[4]*ETH Zürich, CH-8093 Zürich, Switzerland*
[5]*Institut de Física d'Altes Energies (IFAE), The Barcelona Institute of Science and Technology (BIST), E-08193 Bellaterra (Barcelona), Spain*
[6]*Japanese MAGIC Group: Institute for Cosmic Ray Research (ICRR), The University of Tokyo, Kashiwa, 277-8582 Chiba, Japan*
[7]*Technische Universität Dortmund, D-44221 Dortmund, Germany*
[8]*Croatian MAGIC Group: Faculty of Electrical Engineering and Computing (FER), University of Zagreb, 10000 Zagreb, Croatia*
[9]*IPARCOS Institute and EMFTEL Department, Universidad Complutense de Madrid, E-28040 Madrid, Spain*
[10]*Centro Brasileiro de Pesquisas Físicas (CBPF), 22290-180 URCA, Rio de Janeiro (RJ), Brazil*
[11]*Università di Padova and INFN, I-35131 Padova, Italy*
[12]*Faculty of Physics and Applied Informatics, Department of Astrophysics, University of Lodz, PL-90-236 Lodz, Poland*
[13]*Università di Siena and INFN Pisa, I-53100 Siena, Italy*
[14]*Deutsches Elektronen-Synchrotron (DESY), D-15738 Zeuthen, Germany*
[15]*INFN MAGIC Group: INFN Sezione di Torino and Università degli Studi di Torino, I-10125 Torino, Italy*
[16]*Max-Planck-Institut für Physik, D-80805 München, Germany*
[17]*Università di Pisa and INFN Pisa, I-56126 Pisa, Italy*
[18]*ICCUB, IEEC-UB, Universitat de Barcelona, E-08028 Barcelona, Spain*
[19]*Armenian MAGIC Group: A. Alikhanyan National Science Laboratory , 0036 Yerevan, Armenia*
[20]*Centro de Investigaciones Energéticas, Medioambientales y Tecnológicas, E-28040 Madrid, Spain*
[21]*Port d'Informació Científica (PIC), E-08193 Bellaterra (Barcelona), Spain*
[22]*INFN MAGIC Group: INFN Sezione di Bari and Dipartimento Interateneo di Fisica dell'Università e del Politecnico di Bari, I-70125 Bari, Italy*
[23]*Croatian MAGIC Group: Department of Physics, University of Rijeka, 51000 Rijeka, Croatia*
[24]*Universität Würzburg, D-97074 Würzburg, Germany*
[25]*Finnish MAGIC Group: Finnish Centre for Astronomy with ESO, University of Turku, FI-20014 Turku, Finland*
[26]*Ruhr-Universität Bochum, Fakultät fur Physik und Astronomie, AstronomischesInstitut (AIRUB), 44801 Bochum, Germany.*
[27]*Departament de Física, and CERES-IEEC, Universitat Autònoma de Barcelona, E-08193 Bellaterra, Spain*
[28]*Armenian MAGIC Group: ICRANet-Armenia at NAS RA , 0019 Yerevan, Armenia*
[29]*Croatian MAGIC Group: Faculty of Electrical Engineering, Mechanical Engineering and Naval Architecture (FESB), University of Split, 21000 Split, Croatia*
[30]*Croatian MAGIC Group: Department of Physics, Josip Juraj Strossmayer University of Osijek, 31000 Osijek, Croatia*
[31]*Japanese MAGIC Group: RIKEN, Wako, Saitama 351-0198, Japan*
[32]*Japanese MAGIC Group: Department of Physics, Kyoto University, 606-8502 Kyoto, Japan*
[33]*Japanese MAGIC Group: Department of Physics, Tokai University, Hiratsuka, 259-1292 Kanagawa, Japan*
[34]*Dipartimento di Fisica, Università di Trieste, I-34127 Trieste, Italy*
[35]*Saha Institute of Nuclear Physics, HBNI, 1/AF Bidhannagar, Salt Lake, Sector-1, Kolkata 700064, India*
[36]*Inst. for Nucl. Research and Nucl. Energy, Bulgarian Academy of Sciences, BG-1784 Sofia, Bulgaria*
[37]*Finnish MAGIC Group: Astronomy Research Unit, University of Oulu, FI-90014 Oulu, Finland*
[38]*INAF Trieste and Dept. of Physics and Astronomy, University of Bologna*
[39]*Croatian MAGIC Group: Ruđer Bošković Institute, 10000 Zagreb, Croatia*

[40]*INFN MAGIC Group: INFN Sezione di Perugia, I-06123 Perugia, Italy*
[41]*INFN MAGIC Group: INFN Roma Tor Vergata, I-00133 Roma, Italy*
[42]*Dipartimento Interateneo di Fisica dell'Università e del Politecnico di Bari, I-70125 Bari, Italy*
[43]*Instituto de Astrofísica de Andalucía (CSIC), Apartado 3004, E-18080 Granada, Spain*
[44]*INFN Sezione di Perugia, I-06123 Perugia, Italy*
[45]*INAF – Istituto di Radioastronomia, Via Gobetti 101, I-40129 Bologna, Italy*
[46]*Department of Physics and Astronomy, University of Turku, FI-20014 Turku, Finland*
[47]*Università di Siena, I-53100, Siena, Italy.*

This paper has been typeset from a TEX/LATEX file prepared by the author.